Linear modeling of a family of turbulent separation bubbles

C. Cura [1], A. Hanifi [2], A. V. G. Cavalieri [3], and J. Weiss [1]
[1]*Institut für Luft- und Raumfahrt, Technische Universität Berlin, 10587 Berlin, Germany*
[2]*FLOW, Engineering Mechanics, KTH Royal Institute of Technology, 100 44 Stockholm, Sweden*
[3]*Divisão de Engenharia Aeronáutica, Instituto Tecnológico de Aeronáutica, 12228-900 São José dos Campos, São Paulo, Brazil*

(Received 14 July 2025; accepted 9 October 2025; published 13 November 2025)

The low-frequency linear dynamics of a family of incompressible, pressure-gradient (PG)-induced turbulent separation bubbles (TSBs) are studied by means of modal and nonmodal linear analysis. The investigated data consist of Reynolds-averaged Navier-Stokes simulations and experimental measurements that are used for validation purposes. The TSBs are generated on a flat plate by means of adverse (APG) and favorable (FPG) PGs, such that the family of TSBs consists of three distinct cases—small, medium, and large—where the size of the separation bubble is controlled by the strength and location of the maximum APG and FPG. The investigation of the linear dynamics of the family of TSBs reveals two significant results: First, the low-frequency receptivity of the TSB flow, characterized by the low-pass filter behavior of the optimal gain, remains unaffected by the absence of a closed TSB in the time average for the small-sized TSB (small-bubble case). Second, although the large TSB flow is predicted to be globally unstable for a set of spanwise wavenumbers, the amplifier dynamics of the flow appear to dominate over the oscillator dynamics, as evidenced by the persistence of low-frequency unsteadiness in the experimental large-bubble flow. These results suggest that a common physical mechanism, characterized by the stationary, weakly damped global mode, governs the low-frequency unsteadiness across the entire family of TSBs, irrespective of their separation extent or stability characteristics.

DOI: 10.1103/gpdg-42jj

I. INTRODUCTION

Separation bubbles—regions of recirculating flow bounded by the time-averaged lines of separation and reattachment on a solid surface—have been a subject of considerable interest within the fluid dynamics community for several decades. Their wide-ranging implications, including reduced lift, increased drag, noise emission, and structural vibrations, make their complex dynamics a prominent topic of research.

In general, separation bubbles can be classified into several categories based on factors such as the state of the incoming boundary layer, the investigated velocity regime, and the cause of separation. At low speed, a distinction is typically made between laminar separation bubbles (LSBs), which occur over backward facing steps, on flat plates, at the trailing edge of airfoils, or on smooth bumps and ramps [1–3], and turbulent separation bubbles (TSBs), which form under similar geometrical conditions, albeit with a fully turbulent incoming boundary layer [4,5].

Published by the American Physical Society under the terms of the Creative Commons Attribution 4.0 International license. Further distribution of this work must maintain attribution to the author(s) and the published article's title, journal citation, and DOI.

At high speed, when the Mach number reaches the supersonic regime, the separation bubble forms at the shock foot, leading to either laminar or turbulent shock-wave boundary-layer interactions (SBLIs) [6]. Although separation bubbles can also be classified based on their cause, as geometry or pressure-gradient (PG) induced, in the present study, we focus exclusively on the latter. Specifically, we examine TSBs, which arise when a turbulent boundary layer separates from the wall due to an adverse PG (APG) and reattaches again further downstream [7]. Such PG-induced separation bubbles are known to exhibit unsteadiness across a variety of spatial and temporal scales; among these dynamics, a phenomenon that has received significant attention in the recent literature is a low-frequency unsteadiness. In low-speed flows, this unsteadiness manifests as a low-frequency expansion and contraction of the entire separated region and is often referred to as the *breathing* mode of the bubble. It is typically associated with the Strouhal number $\mathrm{St} = fL_b/U_{\mathrm{ref}}$, based on the bubble length L_b and the reference velocity U_{ref} [8]. Values reported in the literature range from $\mathrm{St} \approx 0.01$ to 0.1 for a TSB generated on flat plate by means of a combination of APG and favorable PG (FPG) [9], an APG in the absence of a subsequent FPG [10], a one-sided diffuser flow [11], and the trailing edge of an airfoil [12]. In high-speed flows, a similar low-frequency aperiodic motion is observed at $\mathrm{St} \approx 0.03$, but in this case, it is not only linked to bubble breathing but also with the associated unsteady shock motion [13–16].

Several attempts have been made to explain the origin of the low-frequency unsteadiness in high-speed flows, with implications for subsonic TSBs as well. These explanations generally fall into two categories [15]: upstream mechanisms, where velocity fluctuations in the incoming boundary layer influence the position and size of the separation [17], and downstream mechanisms, either: (a) where inherent instabilities within the flow drive unsteadiness or (b) where instabilities inherent to the flow drive unsteadiness [18–20].

From a modal stability analysis perspective, a key observation in various flows featuring separation bubbles is that the spectral characteristics of the Navier-Stokes operator, linearized around either the base or mean flow, are often governed by a stationary (zero-frequency) leading eigenmode. This stationary mode was found to be globally stable in studies by Bugeat *et al.* [21] in a laminar SBLI, Hao [22] in a turbulent SBLI, and Cura *et al.* [23] in a flow featuring a (subsonic) flat-plate TSB. In the aforementioned works, the stationary leading mode was linked to low-frequency unsteadiness through a forced modal mechanism, driven by this *weakly damped global mode*. Moreover, it has been demonstrated that, when the spectral characteristics are governed by this stable mode, the flow exhibits low-pass filter behavior, preferentially amplifying low-frequency perturbations while attenuating higher-frequency components [21,23].

The existence of such a stationary leading eigenmode, however, does not appear to be exclusive to reattaching flows deemed *globally stable*. Rather, it seems to be an intrinsic and recurrent feature of separation bubbles that can be observed across many velocity regimes, boundary layer states, and geometric conditions. In the laminar regime, Theofilis *et al.* [24] and Rodriguez and Theofilis [25] investigated the global stability of a flow featuring a flat-plate LSB, identifying a three-dimensional (3D) unstable mode. This mode was found to be stationary (zero-frequency) in nature and was linked to the unsteadiness of the separation bubble by Theofilis *et al.* [24], while Rodríguez *et al.* [26] associated it with a centrifugal instability mechanism, leading to the steady three-dimensionalization of the LSB base flow. In a different configuration, this unstable, stationary leading mode was linked to the formation of *stall cells*—3D cellular patterns—on an airfoil wing, driven by a spanwise modulation of the flow induced by this mode [27]. Marquet *et al.* [28] and Gallaire *et al.* [29] studied the modal dynamics of comparable LSB configurations: the flow in a curved channel and forming behind a smooth bump, respectively. A similar 3D, unstable stationary mode was uncovered in both analyses. However, in the work of Marquet *et al.* [28], the transient energy growth of two-dimensional (2D) perturbations was found to be significantly larger at moderate times than the weak exponential growth of the 3D stationary mode. As a consequence, Marquet *et al.* [28] argued that, in the presence of background noise, the amplifier dynamics may dominate over the resonator

dynamics, resulting in the onset of unsteadiness, as frequently observed in experiments, rather than the formation of steady structures.

The unstable stationary mode has been further documented in flows exhibiting a laminar SBLI [30], a turbulent SBLI [31–33], and a TSB on an airfoil wing [34], confirming that it is a recurring feature in separated flows across both laminar and turbulent regimes as well as under subsonic and supersonic conditions. However, whereas the mode was associated with the formation of steady stall cells by Sarras *et al.* [34], Pirozzoli *et al.* [32] and Nichols *et al.* [33] argued that the low-frequency unsteadiness can be modeled as a weakly damped oscillator, as originally proposed by Plotkin [35]. This framework suggests that continuous forcing from the upstream boundary layer may be necessary to maintain the system near a limit cycle [33]. Finally, Sarras [36] studied a flow configuration similar to that of Cura *et al.* [23], where a TSB forms on a flat plate due to an APG, without a FPG downstream of separation. In contrast with our previous work [23], where a weakly damped (marginally stable) mode was identified, the leading stationary mode in the analysis of Sarras [36] was found to be globally unstable. Sarras [36] argues that any flow with a leading stationary eigenmode near marginality will exhibit selective low-frequency amplification, independent of whether the flow is globally stable or unstable. Although this interpretation may be limited by the fact that resolvent analysis (RA) is formally valid only for globally stable flows, it remains consistent with the notion of Marquet *et al.* [28] that, under certain conditions, the exponential growth of the *marginal* mode may be dominated by the transient dynamics of the flow.

In the present work, we extend the analysis of Cura *et al.* [23] to a family of TSBs to investigate whether the previously identified forced modal mechanism, associated with the low-frequency receptivity of TSBs, remains robust at varying degrees of separation. This analysis is motivated by the experimentally observed persistence of low-frequency unsteadiness across different TSB sizes [37]. Following our previous methodology, the linear analyses are performed based on a numerical base flow [38], whereas the experimental measurements of the respective TSB flows [37] are employed for validation purposes. We investigate the modal and nonmodal characteristics of a family of TSBs, where combinations of APG and FPG are used to force a fully turbulent incoming boundary layer to separate and reattach on a flat test surface. The family of TSBs consists of three distinct cases—small, medium, and large—where the size of the separation bubble is controlled by the strength and location of the maximum APG and FPG. Notably, the small TSB flow does not exhibit mean flow separation, while the large TSB flow is found to be globally unstable according to linear theory. As a consequence, the family of TSB flows provides a systematic basis for testing the proposed receptivity mechanism across different degrees of separation and spectral characteristics.

The article is organized as follows. In Sec. II, we introduce the numerical database of Mohammed-Taifour *et al.* [38], which will be used for each respective base flow in the current investigation. In Sec. III, the methodology for the modal and nonmodal analysis is described, followed by a validation of the results for the medium-bubble flow, which was previously studied by Cura *et al.* [23] based on available DNS data, in Sec. IV. The results for the family of TSB flows are then presented in Sec. V before the generality of the proposed mechanism is further examined in Sec. VI. Finally, a conclusion is provided in Sec. VII. Additional details regarding the setup of the linear analysis are provided in the appendixes.

II. NUMERICAL DATABASE

In this section, we introduce the numerical flow database of Mohammed-Taifour *et al.* [38] that will be used in the present study. The database consists of three flow configurations: a small-bubble (SB), a medium-bubble (MB), and a large-bubble (LB) cases. Here, only the setup of the numerical domain as well as the flow solver will be briefly discussed.

The Reynolds-averaged Navier-Stokes (RANS) simulations are designed to reproduce the experimental flow database of Le Floc'h *et al.* [37], where a family of TSBs is generated on a flat-plate test surface by means of a combination of APG and FPG. The numerical domain is designed to match the floor shapes of the experimental test section, leading to the case-distinct APG-FPG distribution

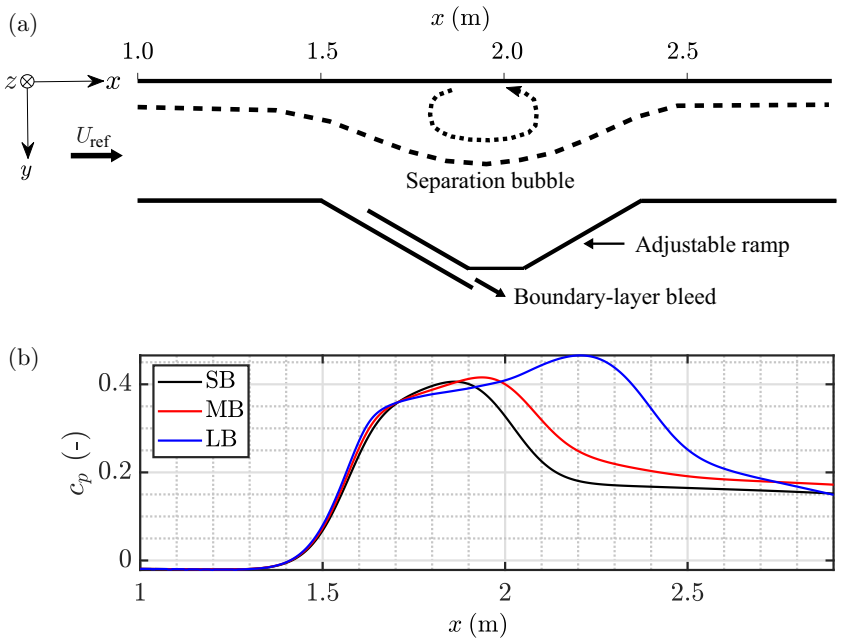


FIG. 1. (a) Schematic of wind-tunnel test section and (b) distribution of pressure coefficient c_p for the SB, MB, and LB cases, EARSM RANS data.

on the top surface. In practice, the position of the adjustable ramp in the downstream portion of the domain is varied to enforce the respective FPG on the top plate. A constant boundary-layer bleed in the upstream part of the domain ensures that the flow remains attached along the bottom wall. A 2D schematic of the wind-tunnel test section is provided in Fig. 1(a). The experimental test section is 3 m in length and 0.6 m in width. In the computational domain, an extension of 0.7 m is added to the incoming zero-PG (ZPG) region to ensure that the incoming turbulent boundary layer at $x = 0$ m matches the experimental data. The spanwise extent of the computational domain is set to $L_z = 0.6$ m. In other words, the finite-span conditions of the experiment (i.e., the side-wall boundaries) are explicitly modeled rather than being replaced by periodic boundary conditions. The resulting wall-pressure coefficient c_p along the top wall is shown in Fig. 1(b). Clearly, the pressure coefficient distributions match up to $x \approx 1.6$ m, after which a more or less distinct plateau is formed, depending on the flow case under consideration.

The base flows employed in the current study consist of steady-state solutions to the incompressible RANS equations using the vertex-based finite volume method from CFX-17.2 on a standard hexahedral mesh (ICEM-CFD). The turbulence model is the baseline explicit algebraic Reynolds stress model (BSL-EARSM), which uses a combination of the Wallin-Johansson explicit algebraic Reynolds stress model (WJ-EARSM) [39] and the baseline (BSL) k-ω model [40]. The validation outlined by Mohammed-Taifour *et al.* [38] demonstrates that the simulations using the BSL-EARSM model provide the closest match to the experimental data. For further details regarding the computational grid, the boundary conditions, etc., see Mohammed-Taifour *et al.* [38].

In the following, for visualization purposes, we will orient the y direction toward the top of the page. The resulting streamwise and wall-normal component of the base flows are depicted in Fig. 2, with the mean flow separation increasing from (a) $L_b = 0$ m (SB) to (b) $L_b = 0.11$ m (MB) to (c) $L_b = 0.47$ m (LB). Note, that a modified domain height is used for the LB case [wall-normal extent, see Fig. 2(c)]. The rationale for and verification of this modified setup will be provided in Sec. IV and Appendix B.

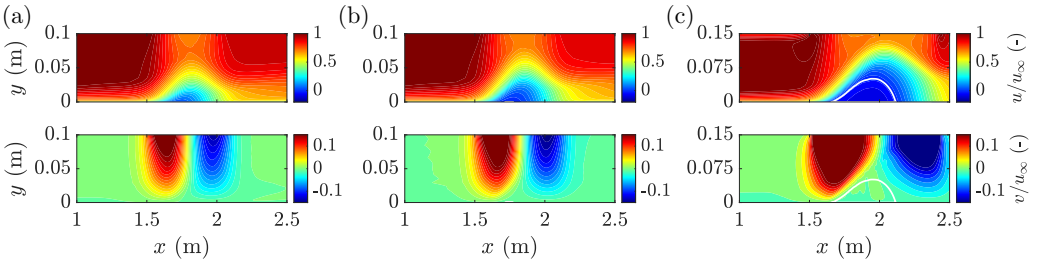


FIG. 2. Streamwise (top) and wall-normal (bottom) components of the TSB base flow. The (a) SB, (b) MB, and (c) LB cases are displayed. The time-average location of the TSB is indicated by the $\overline{u} = 0$ contourline (solid white line). Note the differing wall-normal extent of the (c) LB domain (see Sec. IV and Appendix B).

III. METHODS

In this section, we introduce the governing equations describing the TSB dynamics and briefly outline the stability analysis methods employed in this work. Starting from the viscous incompressible Navier-Stokes equations, we decompose the flow field into time-averaged and fluctuating components according to $\mathbf{q}(x, y, z, t) = \overline{\mathbf{q}}(x, y, z) + \tilde{\mathbf{q}}(x, y, z, t)$. Introducing the above Reynolds decomposition into the incompressible Navier-Stokes equations and time-averaging leads to the linearized Navier-Stokes equations (LNSEs)

$$\begin{aligned} \frac{\partial \tilde{\mathbf{u}}}{\partial t} + \tilde{\mathbf{u}} \cdot \nabla \overline{\mathbf{u}} + \overline{\mathbf{u}} \cdot \nabla \tilde{\mathbf{u}} &= -\nabla \tilde{p} + \nabla \cdot [\nu_T (\nabla \tilde{\mathbf{u}} + \nabla \tilde{\mathbf{u}}^T)] + \tilde{\mathbf{f}}_0, \\ \nabla \cdot \tilde{\mathbf{u}} &= 0. \end{aligned} \tag{1}$$

Here, $\overline{\mathbf{u}} = (\overline{u}, \overline{v}, \overline{w})$ and $\tilde{\mathbf{u}} = (\tilde{u}, \tilde{v}, \tilde{w})$ are the streamwise, wall-normal, and spanwise mean and fluctuating velocity, respectively; $\tilde{p}$ is the fluctuating pressure; and Re is the Reynolds number. As proposed by McKeon and Sharma [41], we group the nonlinear terms in the Navier-Stokes equations into an unknown forcing term $\tilde{\mathbf{f}}_0$ and further represent part of the Reynolds stresses by means of an eddy viscosity model [42], where a total, non-dimensional viscosity $\nu_T = (1 + \nu_t/\nu)/\mathrm{Re}$ is considered.

A. Global linear stability analysis

In the present work, our chosen base flow is a turbulent mean which, strictly speaking, is not consistent with the idea of a global linear stability analysis (GLSA). We are merely inspecting the properties of the Navier-Stokes operator, linearized around the turbulent mean, as has been done for other turbulent flows [43–46]. For clarity and comparability with other studies on turbulent reattaching flows [22,36], we choose to adopt the typical stability nomenclature in the following. However, the reader should keep in mind that our conclusions pertain to the properties of the linearized operator rather than to classical flow stability.

When the forcing term $\tilde{\mathbf{f}}_0$ is dropped in Eq. (1), the asymptotic behavior of the TSB flow can be studied by means of the spanwise periodic eigenvalue problem (EVP)

$$-i\omega \mathbf{M} \hat{\mathbf{q}} = \mathbf{A}_{2D,z} \hat{\mathbf{q}}, \tag{2}$$

where $\beta \in \mathbf{R}$ is the spanwise wave number, $\omega \in \mathbf{C}$ are the eigenvalues, and $\hat{\mathbf{q}}$ are the eigenfunctions. The EVP in Eq. (2) can be analyzed to identify unstable global modes whenever the growth rate $\omega_i > 0$, whereas disturbances decay for $t \to \infty$ when $\omega_i < 0$. The solution to Eq. (2) is computed using the code from Abreu *et al.* [47] and Blanco *et al.* [48], modified for GLSA.

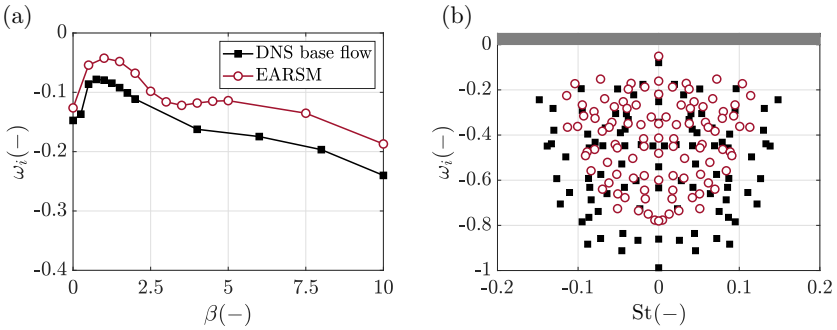


FIG. 3. Validation: (a) Growth rate ω_i of least stable GLSA mode over nondimensional spanwise wave number β and (b) GLSA spectrum for $\beta = 1$. Results presented in Ref. [23] (DNS base flow) and using the EARSM base flow from Ref. [38] (current study) are displayed.

B. Resolvent analysis

To study the forced dynamics of the bubble, we perform RA as described in McKeon and Sharma [41]. For this purpose, we recast Eq. (1) into the resolvent form

$$(-i\omega\mathbf{M} - \mathbf{A}_{2D,z})\hat{\mathbf{q}} = \mathbf{B}\hat{\mathbf{f}}. \tag{3}$$

The optimal response $\hat{\mathbf{q}} = (\hat{u}, \hat{v}, \hat{w})$ to any harmonic forcing $\hat{\mathbf{f}} = (\hat{f}_x, \hat{f}_y, \hat{f}_z, 0)$ can be obtained by performing a singular value decomposition (SVD) of the resolvent operator $\mathbf{R}$

$$\hat{\mathbf{q}} = \mathbf{C}(-i\omega\mathbf{M} - \mathbf{A}_{2D,z})^{-1}\mathbf{B}\hat{\mathbf{f}} = \mathbf{R}\hat{\mathbf{f}}, \tag{4}$$

where $\mathbf{M}$ acts as a masslike matrix, $\mathbf{A}_{2D,z}$ is the 2D LNSE operator [$\overline{\mathbf{u}} = (\overline{u}, \overline{v}, 0)$], and the operators $\mathbf{B}$ and $\mathbf{C}$ act as filters that impose restrictions on the forcing (input) and response (output), respectively. The first singular value of the SVD of the resolvent operator is denoted as the optimal gain σ_1, while the remaining singular values (suboptimal gains) are arranged in decreasing order according to $\sigma_1 > \sigma_2 > \sigma_3 > \ldots > \sigma_n$. The computation of the SVD of Eq. (4) is performed using the code described in Abreu *et al.* [47] and Blanco *et al.* [48]. For details regarding the operators $\mathbf{A}_{2D,z}$, $\mathbf{B}$, $\mathbf{C}$, and $\mathbf{M}$, see Cura *et al.* [23].

IV. VALIDATION OF THE MB CASE

Standard RANS simulations are known to exhibit limitations in the accurate prediction of mean flow separation and reattachment as compared with methods such as direct numerical simulation (DNS). This is particularly true for turbulent flows, where the specific choice of turbulence model may further lead to discrepancies in the turbulent flow quantities. Consequently, their applicability as base flows for linear analyses of turbulent flows may be a subject of debate. Here, we choose to validate our methodology against the modal and nonmodal stability analysis from Cura *et al.* [23] which was based on the DNS of Coleman *et al.* [49] and therefore did not suffer from the limitation of RANS modeling. We select the MB base flow and nondimensionalize all quantities using the length scale $l^* = L_b$ and the timescale $t^* = U_\infty/L_b$. We then perform the modal and nonmodal analysis following the procedure outlined by Cura *et al.* [23].

A. GLSA validation

In Fig. 3, the spectral characteristics of the MB base flow are compared with our previous results using a DNS base flow. We plot the least stable mode over a set of nondimensional spanwise wave numbers $\beta = 2\pi L_b/\lambda$ [Fig. 3(a)]. A similar distribution to that obtained by Cura *et al.* [23] can be observed. However, the maximum of the distribution appears to be slightly shifted toward higher

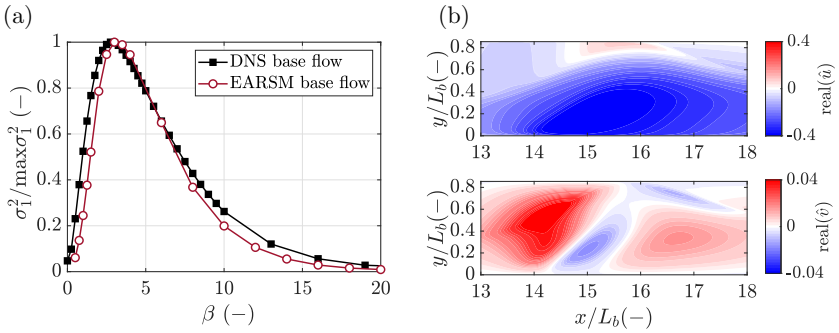


FIG. 4. Validation: (a) Optimal gain $\sigma_1^2/\max(\sigma_1^2)$ over nondimensional spanwise wave number β and (b) streamwise (top) and wall-normal (bottom) component of optimal response at low frequency $\mathrm{St} = 0.01$ and $\beta = 1$ (EARSM data). Results presented in Ref. [23] (DNS base flow) and using the EARSM base flow from Ref. [38] (current study) are displayed.

β. Here, the maximum occurs at $\beta = 1.0$, whereas it is $\beta = 0.75$ for the results obtained using the DNS base flow. The entire curve is further shifted upward, with growth rates ω_i moving closer to the unstable regime. Notably, even though the numerically computed MB data were found to sufficiently match the experimentally measured data [38], discrepancies between the DNS and BSL-EARSM base flows still exist (see Appendix A). Considering this, the agreement between the results obtained using the MB base flow and the results from Cura *et al.* [23] is remarkable. Evidently, the spectral characteristics are not highly sensitive to the exact geometry of the flow. This can be further seen in Fig. 3(b), where the GLSA spectrum is plotted for $\beta = 1$ for both the MB and DNS base flow cases. The stability threshold is indicated by the gray-shaded region. Clearly, both base flows feature similar characteristics. The least damped mode is a stationary ($\mathrm{St} = 0$), globally stable mode. This holds true up to approximately $\beta = 3$, beyond which a traveling ($\mathrm{St} \neq 0$) mode becomes dominant. Similar trends in the stationarity of the leading mode were also observed by Cura *et al.* [23], where the stationary leading mode was associated with the presence of a centrifugal amplification mechanism. Finally, a comparison of the streamwise contours of the leading mode at $\beta = 1$ reveals very similar mode characteristics: a large-scale correlated structure bounding the recirculation region of the bubble (not shown here), which is comparable with the one reported by Cura *et al.* [23].

B. RA validation

We now proceed to analyze the forced dynamics of the MB flow at low frequency ($\mathrm{St} \approx 0.01$) and for several nondimensional spanwise wave numbers β. The optimal energy gain, normalized to take values between 0 and 1, is depicted in Fig. 4(a). Very good agreement between the results obtained using the MB base flow (current study) and our previous results using the DNS base flow can be observed. In both cases, the maximum occurs at $\beta \approx 3$. The experimental data of Cura *et al.* [23] indicated spanwise coherence at $\beta \approx 1$. To stay consistent with Cura *et al.* [23], we depict the streamwise and wall-normal component of the optimal response (MB case) at low frequency $\mathrm{St} = 0.01$ and spanwise wave number $\beta = 1$ in Fig. 4(b). Consistent with our previous findings, the streamwise component features a large elongated structure bounding the recirculation bubble and following its shape. Comparisons of the streamwise and wall-normal component of the optimal response for several spanwise wave numbers β can be found in Appendix A. Finally, the low-pass filter characteristic of the optimal energy gain at low, nonzero spanwise wave numbers β, which was associated with the experimentally measured low-frequency breathing by Cura *et al.* [23], could also be observed using the BSL-EARSM base flow (not shown here).

TABLE I. The flow characteristics of the family of TSBs using the chosen scaling parameters.

	$L_b/Y(-)$	$\mathrm{APG}_{\max}/Y(-)$	$\mathrm{FPG}_{\max}/Y(-)$	$-u_{\mathrm{rev}}/U_\infty(\%)$
SB	0	15.95	19.96	0
MB	1.1	15.84	20.48	0.11
LB	4.7	15.66	23.9	8.19

Overall, the spectral characteristics and the forced dynamics of the flow demonstrate good agreement with our previous findings, even though discrepancies between the MB and DNS base flows are evident (see Appendix A). Clearly, the linear dynamics of the base flow exhibit low sensitivity to small variations in the position and size of the TSB. However, insights gained from a comprehensive analysis of significantly altered TSB shape and size, as will be done in the following sections, are likely to contribute to a deeper understanding of the mechanisms driving the low-frequency breathing phenomenon.

As a reminder, there is no mean flow separation in the SB case, and $L_b = 0\,\mathrm{m}$. Consequently, it was not possible to perform the analysis of the family of TSBs using the same scaling as Cura *et al.* [23]. In the following, to facilitate the comparison across the different TSB configurations, we adopt a fixed scaling based on the domain height $Y = 0.1\,\mathrm{m}$ and the freestream velocity $U_\infty = 25\,\mathrm{ms}^{-1}$. The chosen reference height Y captures the dominant shear regions in both the SB and MB cases [see Figs. 2(a) and 2(b)]. For the LB case, where the TSB extends beyond Y [see Fig. 2(c)], a higher wall-normal extent $y_h = 0.15\,\mathrm{m}$ is required to ensure full spatial resolution of the dominant modes. As shown in Appendix B, this adjustment has negligible effect on the leading mode dynamics. The discussion on alternative scaling parameters will be revisited in Sec. VI.

V. FAMILY OF TSBS DYNAMICS

We begin this section with a short overview of the flow characteristics of our family of TSBs using the chosen scaling parameters $l^* = Y$, $t^* = U_\infty/Y$. In this scaling, the SB case displays no mean flow separation, and $L_b/Y = 0$ (see Table I). The subsequent cases, display a medium-sized TSB with $L_b/Y = 1.1$ (MB) and a large TSB with $L_b/Y = 4.7$ (LB). In the nondimensional coordinate system $x^* = x/Y$, $y^* = y/Y$, the position of maximum APG is approximately constant at $x^* = 16$, and the position of maximum FPG increases from $x^* \approx 20$ (SB) to 20.5 (MB) and finally to 24 (LB). Further, the peak reversed flow in percentage of the freestream velocity is also provided in Table I.

A. Modal dynamics

In Fig. 5(a), the least stable mode of the global LSA is plotted for the small, medium, and large TSB base flows, respectively. Several nondimensional spanwise wave numbers $\beta^* = 2\pi Y/\lambda$ (note the different scaling with the height of the domain Y instead of with the bubble length L_b [23]) are considered. The corresponding real part of the eigenvalue $f^* = \omega_r/2\pi$ is displayed in Fig. 5(b). Based on our previous work (and the validation displayed above), we expect the MB case to be globally stable for all β^*, with the maximum located at low, nonzero β^*. Cura *et al.* [23] associated this weakly damped mode with a centrifugal amplification mechanism of the bubble, driving the low-frequency receptivity of the flow. The weakly damped ($\omega_i < 0$), 3D ($\beta^*_{\max} \neq 0$), and stationary ($f^* = 0$) character of the least stable mode of the MB base flow is confirmed here in Fig. 5(a). We further see in Fig. 5(b) that the least stable mode remains stationary ($f^* = 0$) up until $\beta^* \approx 3.5$, after which it becomes a traveling mode ($f^* \neq 0$).

The effect of completely suppressing the mean flow separation, while simultaneously retaining the PG characteristics, can be observed in Figs. 5(a) and 5(b) for the SB case. Interestingly, even though $L_b/Y = 0$, both the growth rate of the least stable mode as well as the nondimensional

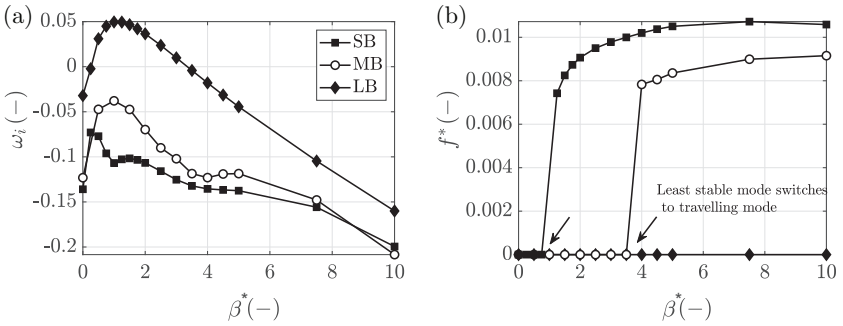


FIG. 5. (a) Growth rate of least stable GLSA mode and (b) nondimensional frequency $f^* = \omega_r/(2\pi)$ of least stable mode over nondimensional spanwise wave number β. The SB, MB, and LB cases are displayed, respectively.

frequency f^* of the respective mode share strong qualitative similarities with the MB case. A maximum of the growth rate at low, nonzero spanwise wave number can be observed well within the stable regime $\beta^* = 0.25$, whereas the switch from stationary to traveling mode now occurs at $\beta^* = 0.75$. As a consequence, it appears that the spectral characteristics of the TSB flow remain mostly unaffected by the absence of a time-averaged separation bubble. Reducing the size of the TSB from $L_b/Y = 1.1$ to 0 merely shifts the maximum of ω_i, as well as the switch in stationarity, to lower β^*. At the same time, a reduction in TSB size has a stabilizing effect on the flow. This observation is consistent with the literature since the peak reversed flow is $0u_\infty$ for the SB case. On the contrary, the effect of massively increasing the TSB size can be observed in Figs. 5(a) and 5(b) for the LB case. The mean separation length is now $L_b/Y = 4.7$, and the peak reversed flow is $-0.08u_\infty$. Immediately, a key distinction becomes evident: several spanwise wave numbers β^*, within the range 0.5–3, now exhibit growth rates in the unstable regime ($\omega_i > 0$). Interestingly, aside from this shift, the distribution of growth rates and their corresponding nondimensional frequencies appear to be scaled versions of those observed in the SB and MB cases. We observe stationary modes for all displayed β^*, with the shift to traveling modes substantially delayed to higher values of β^* (not shown here).

In Fig. 6, we plot the streamwise component of the leading mode at $\beta^* = 0.25$. This value is close to the maximum growth rate for the SB and MB cases and within the stable and stationary region for all considered TSB flows. Clearly, all modes share similar characteristics. A large coherent structure can be observed in the region of the bubbles (MB, LB) or, in the SB case, in the velocity-deficit region. From top to bottom, that is, with increasing bubble size, this coherent structure detaches from the wall and increases in amplitude (note that we scale the modes to take values between -1 and 1 to allow for a common colormap). The origin of the maximum appears to be roughly constant at $x^* = 16$, which is the position of the maximum APG, see Table I. Further, the orientation of the maximum of the mode appears to be well aligned with the region of highest shear. This was confirmed by comparing contours of the vorticity $\omega_z = \partial V/\partial x - \partial u/\partial y$ with the global modes in Fig. 6. For this purpose, we depict the height of the maximum vorticity for each streamwise position (black dashed line) as well as the contour of $0.95\omega_{z,\max}$ (black solid line).

To investigate whether the transition from stable to unstable mode is accompanied by significant changes in the spectral characteristics of the linearized Navier-Stokes operator, we depict the eigenvalue spectra for selected spanwise wave numbers in Fig. 7. From top to bottom, the SB [Fig. 7(a)], MB [Fig. 7(b)], and LB [Fig. 7(c)] cases are displayed, respectively. Two nondimensional spanwise wave numbers β^* are shown, 0.25 (stable regime) and 1.0 (LB case unstable). For $\beta^* = 0.25$, we identify the leading stationary mode (S1) as well as the leading traveling mode (T1) in each subfigure [Figs. 7(a)–7(c)]. First, we consider the stable regime ($\beta^* = 0.25$), which was also depicted in terms of the streamwise component of the leading global mode in Fig. 6. In concordance

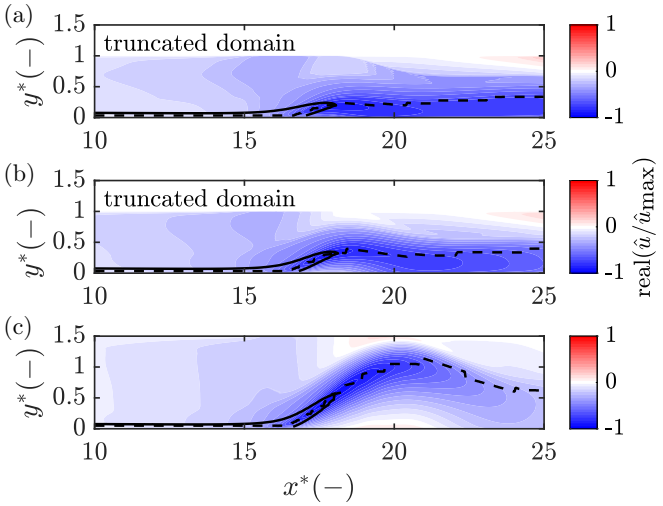


FIG. 6. Streamwise component of leading stationary mode for $\beta^* = 0.25$. The SB, MB, and LB cases are displayed in the top, center, and bottom, respectively. We depict the height of the maximum vorticity $\omega_z = \partial V/\partial x - \partial u/\partial y$ for each streamwise position (black dashed line) as well as the contour of $0.95\omega_{z,\max}$ (black solid line). Note the truncated vertical extent for cases SB and MB. The amplitude is scaled using max[real($\hat{u}$)] to allow for a common colormap.

with Fig. 5(b), a leading stationary mode (S1) is evident in all subfigures [Figs. 7(a)–7(c)]. As the bubble size increases, the spatial separation between the leading stationary mode (S1) and the subleading traveling mode (T1) becomes more pronounced. Whereas the leading stationary mode (S1) is substantially damped in the SB case for $\beta^* = 1$ (leading modes are now $f^* \neq 0$), the overall structure of the spectrum remains the same for the MB and LB cases.

Overall, the results suggest a certain degree of generality in the spectral characteristics of the modes. That is, while the stationary leading mode exists [see Fig. 5(b)], qualitative similarity in the spectral shape becomes apparent. As the bubble size increases, this leading mode grows in dominance, showing greater spatial separation from the subleading modes over a specific range of β^*. In the LB case, the stationary mode becomes sufficiently strong to transition into the unstable regime, where it is accompanied by a second, subleading stationary mode that remains in the stable region. Notably, the position, phase, and shape of each corresponding leading mode (SB, MB, and LB) remain consistent in the vicinity of $\beta^* \sim 1$, even as the growth rate enters the unstable domain ($\omega_i > 0$) in the LB case (not shown here). This suggests that a similar governing mechanism might be at play in all cases, with the stationary leading mode acting as its defining and driving factor.

B. Instability thresholds for TSBs

In studies of LSB flows, the onset of absolute instability has been associated with a threshold level of peak reversed flow, typically in the range of $-u_{\text{rev}}/u_\infty = 16$–$25\%$ [50–52]. However, Rodríguez *et al.* [26] demonstrated that significantly lower values, as small as $-u_{\text{rev}}/u_\infty \approx 10\%$, may lead to 3D instability, which was attributed to a centrifugal amplification mechanism. To our knowledge, no prior attempts have been made to determine a similar threshold for the onset of instability in TSBs. In this section, we seek to establish a similar instability threshold for TSBs, following the classical approach based on a characteristic quantity of the flow. Two quantities are considered, the peak reversed flow u_{rev} and the bubble length L_b. To bridge the gap in our data—where the medium flow exhibits only 0.1% peak reversed flow, while the large TSB reaches 8%—we adopt the approach of Lajús Jr. *et al.* [53] and Yuan *et al.* [54], where a continuous variation of the mean flow is employed

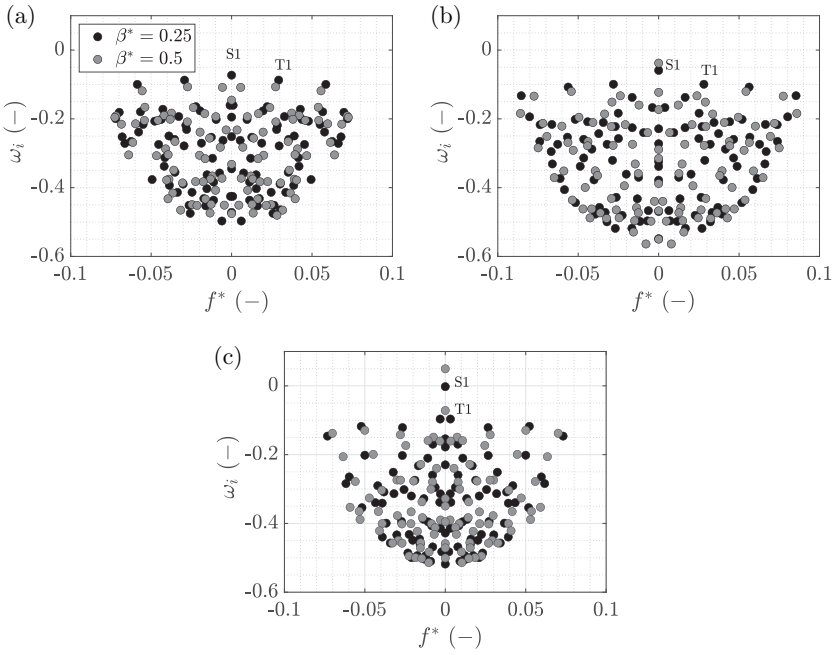


FIG. 7. GLSA spectrum for the nondimensional spanwise wave number $\beta^* = 0.25$ (black) and $\beta^* = 1.0$ (gray). The (a) SB, (b) MB, and (c) LB cases are displayed, respectively.

to generate synthetic base flows for stability analysis. A linear combination of the MB and LB base flows is obtained as

$$\overline{\mathbf{U}}_{\text{synth}} = (1-\kappa)\overline{\mathbf{U}}_{\text{MB}} + \kappa\overline{\mathbf{U}}_{\text{LB}}, \tag{5}$$

where the blending factor κ takes values between 0 (MB case) and 1 (LB case). From the previous sections, we know that the TSB mean flow becomes globally unstable according to the linear theory within the range $0 < \kappa < 1$. Hence, we generate nine synthetic base flows for $\kappa \in [0.1, 0.9]$ with increments of $\Delta\kappa = 0.1$. For completeness, examples of the thus created synthetic base flows for $\kappa = 0.3$, 0.6, and 0.9 are provided in Appendix C. In Fig. 8, we present the growth rate ω_i over the nondimensional spanwise wave number β^* for several blending factors κ [Fig. 8(a)] as well as the eigenvalue spectrum for $\beta^* = 0.5$ [Fig. 8(b)]. An increase in TSB size ($\kappa \to 1$) is represented by a progressively darker shading of the symbols. As described above, the LB case ($\kappa = 1$) appears to be a stronger variation of the MB case ($\kappa = 0$). The growth rate of the leading mode in Fig. 8(a) increases smoothly, though the extent of this increase varies across spanwise wave numbers. Notably, the growth rate exhibits almost linear dependence on κ for nonzero spanwise wave numbers around $\beta^* \sim 1$ [e.g., see Fig. 8(b)]. For each synthetic base flow and its corresponding blending factor κ, we compute the peak reversed flow u_{rev} in percentage of the freestream velocity, along with the bubble length L_b. We plot contours of the growth rate ω_i of the leading mode over spanwise wave number and reverse flow in Fig. 9(a) and over spanwise wave number and bubble length in Fig. 9(b). The exact combinations of (β^*, u_{rev}) or (β^*, L_b) of the stability analyses are indicated by black symbols in the figures. The unstable region is enclosed by a black solid line.

Growth rates $\omega_i > 0$ are achieved for spanwise wave numbers $\beta^* \sim 1$ and $u_{\text{rev}} = 1.1$–$8.2\%u_\infty$ [Fig. 9(a)] and $L_b > 0.2\,\text{m}$ [Fig. 9(b)]. Notably, these values are significantly lower than the thresholds reported for absolute instability in LSBs, suggesting that global instability in TSBs may emerge at much lower reverse flow levels or bubble lengths. However, as shown in our previous analysis [23], the stationary global mode, in the absence of forcing, cannot account for

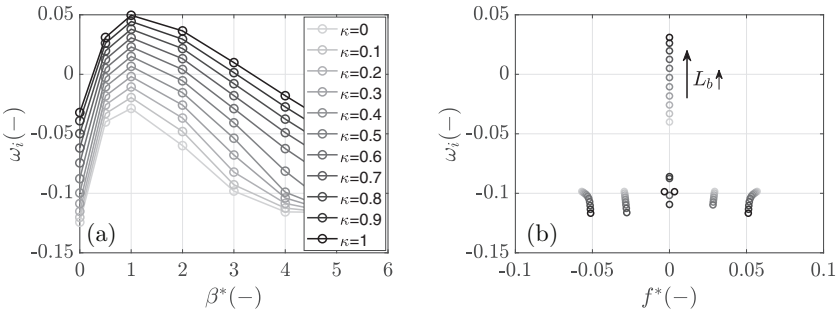


FIG. 8. (a) Growth rate ω_i over nondimensional spanwise wave number β^* and (b) eigenvalue spectrum for $\beta^* = 0.5$. The MB case ($\kappa = 0$), the LB case ($\kappa = 1$), as well as nine synthetic solutions for $\kappa \in [0.1, 0.9]$ are displayed. An increase in TSB size is represented by a progressively darker shading of the symbols.

the experimentally observed broadband low-frequency unsteadiness. Even when globally unstable, the stationary nature of the mode may imply a steady three-dimensionalization of the flow rather than the observed low-frequency dynamics. To investigate the selective low-frequency receptivity to low-frequency perturbations in the family of TSBs, we now perform RA.

C. Forced dynamics

RA is typically performed for asymptotically stable flows, where the eigenvalues of the Navier-Stokes operator, linearized around a base or mean flow, satisfy $\omega_i < 0$. In such cases, the resolvent operator $\mathbf{R}(\omega) = (-i\omega\mathbf{M} - \mathbf{A}_{2\mathrm{D},z})^{-1}$ is well defined for all real forcing frequencies $\omega \in \mathbf{R}$, and the optimal response to any harmonic forcing can be studied by performing the SVD of the resolvent operator. If the flow is globally unstable, at least one eigenvalue will satisfy $\omega_i > 0$, and the resolvent operator becomes unbounded as the forcing frequency approaches ω_i. Guided by the hypothesis that the LB case constitutes a more pronounced manifestation of the forced modal mechanism responsible for the low-frequency unsteadiness of the medium-sized separation bubble [23], we demonstrate that the forced dynamics for flow parameters leading to linearly stable behavior (i.e., spanwise wave numbers with linearly stable eigenvalues) already capture the relevant low-frequency behavior.

With the restriction imposed that we do not perform RA for the LB case and for values of $\beta^*(\omega_i > 0)$, we present the streamwise (top) and wall-normal (bottom) components of the optimal

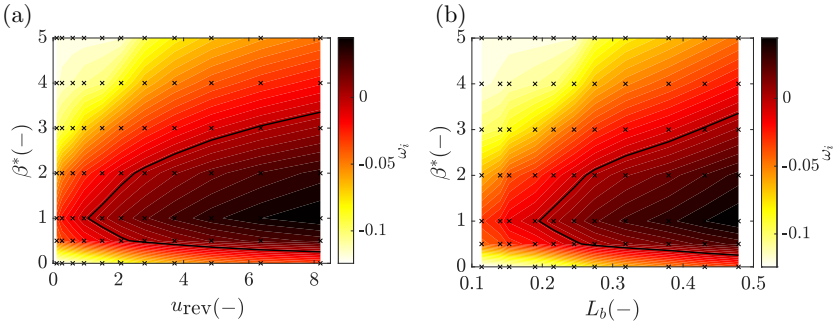


FIG. 9. (a) Contours of growth rate ω_i as a function of the nondimensional spanwise wave number β^* and the peak reversed flow u_{rev} and (b) the nondimensional spanwise wave number β^* and the bubble length L_b. Synthetic data following Eq. (5) are depicted. The computed combinations of (β^*, u_{rev}) and (β^*, L_b) of the stability analyses are indicated by symbols. The unstable region $\omega_i > 0$ is enclosed by a black solid line.

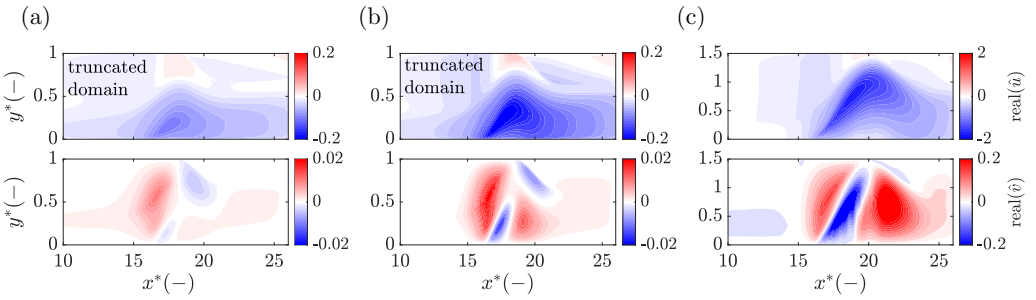


FIG. 10. Streamwise (top) and wall-normal (bottom) component of optimal response for nondimensional spanwise wave number $\beta^* = 0.25$ and low frequency St ≈ 0.01. The (a) SB, (b) MB, and (c) LB flows are displayed, respectively. Note the truncated vertical extent for cases SB and MB and the amplitudes for case LB, which are one order of magnitude larger than for cases SB and MB (differing colormap limits).

response at low frequency ($f^* \approx 0.01$) for the spanwise wave number $\beta^* = 0.25$ in Fig. 10. Results are shown for the SB [Fig. 10(a)], MB [Fig. 10(b)], and LB [Fig. 10(c)] cases. Note that the streamwise and wall-normal component of the RA modes of case LB are one order of magnitude larger than for cases SB and MB (differing colormap limits). The streamwise component of the modes (top) exhibits characteristics that closely resemble those of the streamwise component of the stationary global modes (Fig. 6). In the SB case [Fig. 10(a)], the maximum of the streamwise component is located close to the wall. It increases in magnitude as the bubble size grows and shifts away from the wall. This behavior was previously linked to the alignment of the mode with the region of highest shear in the flow (see Sec. V A). In our previous work [23], in which we investigated the MB case using a DNS base flow, the strong similarity between the leading GLSA modes and optimal response of RA was interpreted as evidence that the low-frequency receptivity is associated with a forced modal mechanism, driven by a weakly damped global mode. Our results indicate that the same forced modal mechanism may be present across all investigated TSBs (SB, MB, and LB), with the response amplitude increasing progressively with bubble size.

The optimal energy gain σ_1^2 of RA for several nondimensional frequencies f^* is shown in Fig. 11(a). The presented results correspond to the nondimensional spanwise wave number $\beta^* = 0.25$, which was shown to coincide with globally stable stationary modes for all considered TSB flows in Sec. V A. Notably, the receptivity of all investigated base flows is characterized by a broadband low-pass filter function, where low-frequency disturbances are selectively amplified, while higher-frequency components are attenuated (see also Fig. 14 in Ref. [23]). These

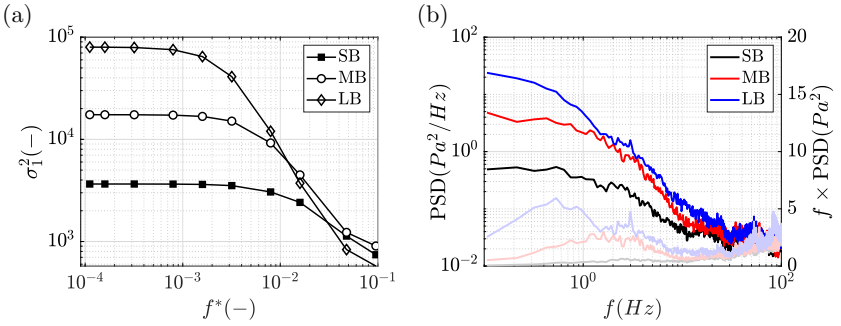


FIG. 11. (a) Optimal energy gain σ_1^2 over different nondimensional frequencies f^* and $\beta^* = 0.25$ and (b) classical and premultiplied PSD of unsteady wall-pressure measurements at $x = 1.6$ m computed from data of Le Floc'h *et al.* [37]. The SB, MB, and LB cases are displayed.

findings align with the experimental results of Mohammed-Taifour and Weiss [55], who related the low-frequency oscillations of the separation and reattachment fronts of the large TSB to the aforementioned low-pass-filter characteristic of the bubble. The transfer function in Fig. 11(a) increases in amplitude with increasing bubble size, whereas the cutoff frequency of the low-pass filter takes the highest values for the SB case and continuously decreases to the value of the LB case. A similar inverse relationship between the size of the bubble and the breathing frequency was observed experimentally in Le Floc'h *et al.* [37], where unsteady wall-pressure measurements along the test-section centerline were performed for the SB, MB, and LB cases. In Fig. 11(b), we depict the classical log-log power spectral density (PSD) as well as the premultiplied PSD of unsteady wall-pressure measurements near the position of maximum APG ($x = 1.6\,\mathrm{m}$). Both, the low-frequency hump (premultiplied PSD) and log-log representation indicate that the cutoff frequency of the forced dynamics diminishes as the bubble size increases.

Interestingly, the presence of a time-averaged separation bubble does not seem to be a prerequisite for the manifestation of the low-pass-filter characteristic, as the SB flow still displays this behavior despite the absence of mean flow separation ($L_b/Y = 0$, see Table I).

D. Alignment with experimental data

To validate our hypothesis, we quantify the alignment [56,57] between the leading spectral proper orthogonal decomposition (SPOD) mode and the optimal response of RA at low frequency (LB, stable flow). For this purpose, we compute the alignment metric

$$\varphi = \frac{\langle \hat{\boldsymbol{q}}_{1_{\mathrm{SPOD}}}, \hat{\boldsymbol{q}}_{1_{\mathrm{RA}}} \rangle}{\|\hat{\boldsymbol{q}}_{1_{\mathrm{SPOD}}}\| \cdot \|\hat{\boldsymbol{q}}_{1_{\mathrm{RA}}}\|}, \tag{6}$$

where $\langle \cdot, \cdot \rangle$ is the L_2 inner product and $\| \cdot \|$ is the euclidean norm. Le Floc'h *et al.* [37] performed time-resolved particle image velocimetry (TR-PIV) measurements in the streamwise/wall-normal plane on the centerline of the test section ($z = 0\,\mathrm{m}$). The measurements consist of five overlapping fields of view of $225 \times 75\,\mathrm{mm}$ (x-y). Three successive time series of $N_t = 3580$ snapshots were taken at an acquisition rate of $f_s = 900\,\mathrm{Hz}$, respectively. For convenience, these measurement planes will be referred to as (streamwise) stations 1–5 in the following.

Given that the high-speed PIV measurements were performed in a planar configuration, no spanwise velocity component was measured. Consequently, the alignment metric consists of the projection of the first SPOD mode $\hat{\boldsymbol{q}}_{1_{\mathrm{SPOD}}} = [\hat{u}_{1_{\mathrm{SPOD}}}, \hat{v}_{1_{\mathrm{SPOD}}}]$ on the first resolvent mode $\hat{\boldsymbol{q}}_{1_{\mathrm{RA}}} = [\hat{u}_{1_{\mathrm{RA}}}, \hat{v}_{1_{\mathrm{RA}}}]$, where $\hat{u}_1$, $\hat{v}_1$ are the streamwise and wall-normal components of the SPOD and resolvent mode, respectively.

The SPOD was performed using the algorithm proposed by Towne *et al.* [58]. For this purpose, the data were split into blocks of $N_{\mathrm{FFT}} = 512$ with 50% overlap, where overlapping blocks between consecutive uncorrelated runs were removed. To address the arbitrariness of the phase of the computed modes, we set the phase of the wall-normal component of the leading mode $\hat{v}$ to zero, while $|\hat{v}| = 1$ [23] at the global reference position $(x^*, y^*) = (19.5, 0.5)$ (SPOD station 3). Continuity across stations is then enforced using a simple stitching procedure following Schmidt and Colonius [59], where multiplication by a complex constant aligns phase and amplitude at fixed points $\vec{P}_{ij}$ in the regions of overlap between consecutive stations (i.e., $\vec{P}_{12}$ is chosen for stations 1 and 2).

We present the streamwise component of the leading low-frequency SPOD mode for each respective field of view (stations 1–5) in Fig. 12 (top), alongside the corresponding portion of the resolvent mode (bottom; note that the wall-normal extent of the plots it restricted to the region captured by the TR-PIV measurements, which is substantially smaller than the full RA domain). Clearly, the SPOD and resolvent modes exhibit significant similarities, particularly at the first four stations. Here, the mode shapes and the locations of extreme values are very well aligned, with alignment values exceeding 94% for stations 1–4 (see Table II).

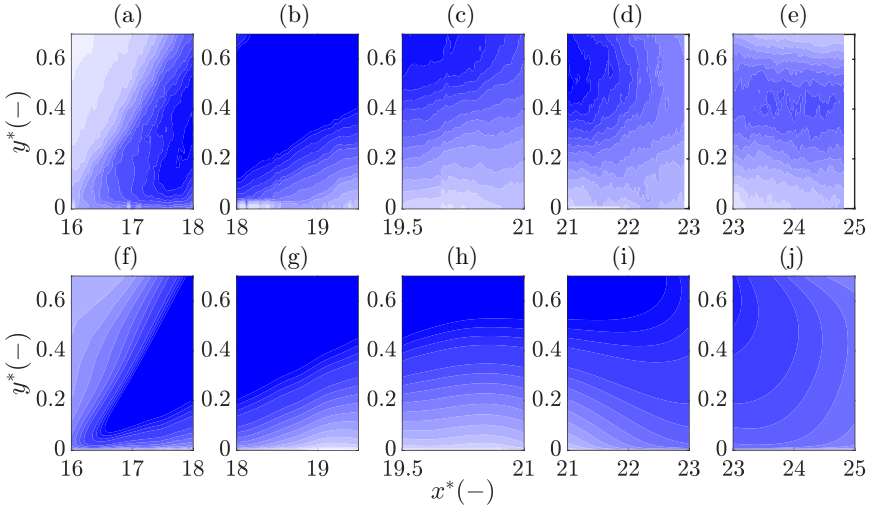


FIG. 12. (a)–(e) Leading SPOD mode of the fluctuating streamwise velocity from experiments and (f)–(j) optimal response of RA. Results at low frequency and for $\beta^* = 0.25$ are depicted. All modes are scaled according to $|\hat{v}| = 1$ and $\arg(\hat{v}) = 0$ at the nondimensional position $x^* = 19.5$ and $y^* = 0.5$. Note that the wall-normal extent of the plots is restricted to the region captured by the TR-PIV measurements, which is substantially smaller than the full RA domain.

TABLE II. Alignment φ between the leading SPOD mode and optimal response from RA at low frequency. The nondimensional spanwise wave number $\beta^* = 0.25$ and five streamwise stations are considered.

	Station 1	Station 2	Station 3	Station 4	Station 5
Alignment $\varphi(-)$	0.95	0.97	0.98	0.95	0.91

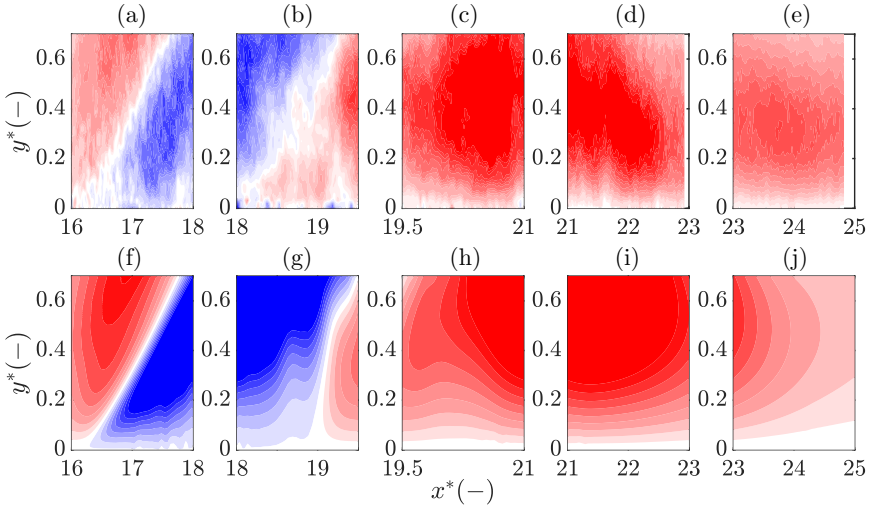


FIG. 13. (a)–(e) Leading SPOD mode of the fluctuating wall-normal velocity from experiments and (f)–(j) optimal response of RA. Results at low frequency and for $\beta^* = 0.25$ are depicted. All modes are scaled according to $|\hat{v}| = 1$ and $\arg(\hat{v}) = 0$ at the nondimensional position $x^* = 19.5$ and $y^* = 0.5$. Note that the wall-normal extent of the plots is restricted to the region captured by the TR-PIV measurements, which is substantially smaller than the full RA domain.

Similar trends can be observed in Fig. 13, where the wall-normal component of the low-frequency SPOD and resolvent modes are displayed. However, it appears that RA slightly overpredicts the streamwise extent of the breathing mode, which leads to reduced levels of alignment at the remaining station 5. Nonetheless, even at this station, the alignment still exceeds 90%, indicating that the experimentally measured breathing mode and the optimal response of RA at low frequency are exceptionally well aligned. Moreover, achieving the highest alignment at station 3 is expected, as the phase and amplitude of the wall-normal component of SPOD and RA modes were linked for this streamwise station.

VI. DISCUSSION

The results presented so far demonstrate that the forced modal dynamics, characterized by the global LSA and RA modes, are qualitatively similar across the entire family of TSBs. Specifically, the existence of a closed TSB in the time average does not seem to be a prerequisite for the manifestation of forced low-frequency receptivity. Instead, the PG characteristics and the resulting curvature of streamlines appear sufficient to drive a selective low-frequency amplification, consistent with the centrifugal amplification mechanism proposed by Rodríguez *et al.* [26] for LSBs. Moreover, the emergence of global instability (LB case) for certain spanwise wave numbers (e.g., at $\beta^* = 0.5$) does not appear to prevent the occurrence of low-frequency receptivity (see Fig. 11). This observation aligns with the findings of Marquet *et al.* [28], who studied the amplifier and resonator dynamics of a curved-channel LSB and demonstrated that the transient growth of disturbances, at moderate times, could significantly outweigh the weak exponential growth of a similar stationary instability. In the following, we examine the generality of the forced amplification mechanism using the framework introduced by Bugeat *et al.* [21] for the low-frequency unsteadiness of laminar SBLIs, which supports the notion that low-frequency receptivity arises from marginal stability and mode stationarity [21,23,36]. Finally, we seek to identify a physically meaningful scaling parameter that collapses the cutoff frequency associated with low-frequency unsteadiness across the family of TSB flows considered.

A. Modal amplification model

In the literature, the low-frequency unsteadiness observed in (turbulent) reattaching flows featuring separation bubbles is often interpreted through the lens of either *upstream* or *downstream* mechanisms [15]. This dichotomy typically implies that either global stability analysis—representing downstream, resonator-type mechanisms—or RA—representing upstream, amplifier-type mechanisms—can independently account for the origin of the low-frequency breathing observed in TSBs. However, our findings indicate that the global mode, in the absence of forcing, is insufficient to account for the low-frequency unsteadiness (see also Cura *et al.* [23]). Conversely, RA, when performed without the guidance of GLSA, may fail to reveal the forced modal character of the observed dynamics. To clarify the concepts of amplification in RA, we recall that the response of a linear system to harmonic forcing can be large due to two main reasons: The forcing frequency is close to an eigenvalue of the linear operator (resonance), or the linear operator has a set of highly nonorthogonal eigenvectors, allowing for a large response even when the forcing is off-resonance [60]. Building on this general concept, we show that the observed low-frequency receptivity of the family of TSBs arises from the stationary, near-resonant ($\omega_i \approx 0$) global mode [21,34]. We adopt the low-pass-filter model proposed by Bugeat *et al.* [21] for the low-frequency unsteadiness of a flow featuring a laminar SBLI. In this model, it was argued that, when the optimal gain is driven exclusively by modal effects, the resolvent gain is governed primarily by the distance d between the forcing frequency f^* and the eigenvalue $\omega = \omega_r + i\omega_i$ of the global mode in the complex plane [21]

$$d = \sqrt{\left(f^* - \frac{\omega_r}{2\pi}\right)^2 + \left(\frac{\omega_i}{2\pi}\right)^2}. \tag{7}$$

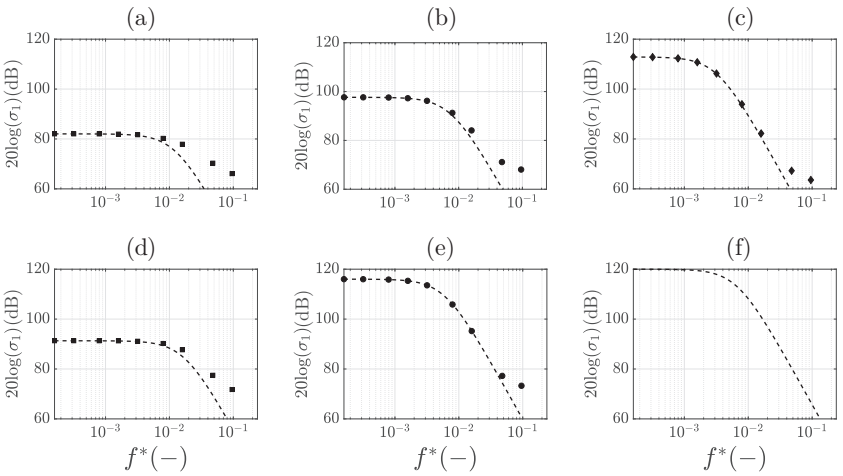


FIG. 14. Low-pass filter representation of optimal gain from RA $20\log(\sigma_1)$ for the (a) and (d) SB, (b) and (e) MB, and (c) and (f) LB cases. Two nondimensional spanwise wave numbers are depicted: (a)–(c) $\beta^* = 0.25$ (all cases globally stable) and (d)–(f) $\beta^* = 1$ (LB case globally unstable). The low-pass-filter model from Bugeat *et al.* [21] (dashed lines) and the results from RA (symbols) are displayed, respectively.

Then the optimal gain should exhibit the behavior $\sigma \sim 1/d$. Given that the eigenvalue of the leading GLSA mode is purely imaginary, the optimal gain can thus be expressed as

$$\sigma_{\text{model}} \sim \frac{1}{\sqrt{1 + \left(\frac{f^*}{\omega_i/2\pi}\right)^2}}. \tag{8}$$

In Fig. 14, we present results from the RA (symbols) of the SB [Figs. 14(a) and 14(d)], MB [Figs. 14(b) and 14(e)], and LB [Figs. 14(c) and 14(f)] cases. The low-pass-filter representation $20\log(\sigma_1)$ is chosen to emphasize the first-order low-pass-filter character of the gain (see also fig. 14 in Cura *et al.* [23]). The model from Eq. (8) [21] is indicated in each subfigure by a black-dashed line. Two nondimensional spanwise wave numbers are depicted: $\beta^* = 0.25$ [Figs. 14(a)–14(c)], for which the LB base flow is predicted to be globally stable according to linear theory, and $\beta^* = 1.0$ [Figs. 14(d)–14(f)], where the LB base flow is globally unstable. Consequently, the low-frequency receptivity in Fig. 14(f) is only estimated by the model, which does formally not distinguish between globally stable ($\omega_i < 0$) or unstable ($\omega_i > 0$) eigenvalues.

Evidently, the low-frequency receptivity of the family of TSBs is well predicted by the leading GLSA mode for both spanwise wave numbers considered, $\beta^* = 0.25$ and 1.0. The optimal gain from the RA exhibits progressively closer agreement with the low-pass-filter model as the bubble size grows (left to right) or when the spanwise wave number is moderately increased [Figs. 14(d)–14(f)]. The first aspect may pertain to the strength of the low-frequency unsteadiness, which appears to be related to the size of the TSB, as evidenced by the trends observed in Secs. V A and V C. The latter is associated with the presence of Kelvin-Helmholtz (KH) rollers, which are typically linked to the medium-frequency shedding of vortices from the shear layer bounding the recirculation region in flows exhibiting TSBs (see Cura *et al.* [23]).

The observation that low-frequency receptivity, associated with the low-frequency breathing motion of TSBs, is accurately predicted by the purely modal low-pass-filter model strongly supports the main hypothesis of this work. The low-frequency unsteadiness in TSBs is most likely governed by a forced modal mechanism driven by a stationary leading global mode. Interestingly, the reported receptivity persists independently of whether a closed TSB is present in the mean flow (SB case) or whether a weak global instability emerges (LB case). Notably, similar leading stationary modes have

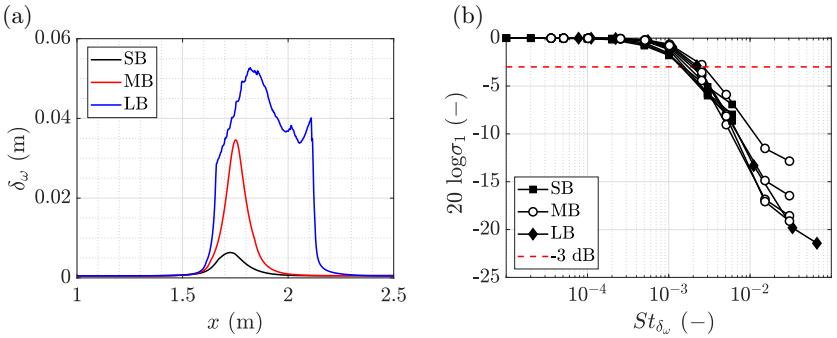


FIG. 15. (a) The vorticity thickness $\delta_\omega(x)$ for the SB, MB, and LB cases. (b) Scaled low-pass-filter representation of the optimal gain of RA $20\log(\sigma_1)(-)$ for spanwise wave numbers $\beta^* = 0.25, 0.5, 1.0,$ and 1.5 and the SB, MB, and LB cases. Only $\beta^* = 0.25$ is depicted for the LB case (stable flow). The curves are scaled using the maximum vorticity thickness $\max(\delta_\omega)$. The maximum of each curve is subtracted to shift the curves to 0dB. The -3dB line is then indicated as a red dashed line.

been identified in various flows featuring separation bubbles, both in the subsonic and supersonic regimes, suggesting that a similar mechanism may be responsible for the low-frequency dynamics across different flow scenarios. Although the global instability reported in this work does not change the fundamental character of the observed low-frequency dynamics, it may, under certain conditions, lead to the formation of steady 3D structures, such as stall cells, which could compete with or suppress transient growth. However, an in-depth analysis of this potential mechanism falls outside the scope of the present study and warrants further investigation in future work.

B. Shear mechanism: Scaling with δ_ω

Up to this point, all the reported results were scaled using the small domain height Y and the freestream velocity U_∞. As indicated earlier, this was a practical choice, given that we did not know *a priori* which scaling to adopt, and the classical scaling based on the bubble length L_b [8] was not available (i.e., $L_b = 0$ m in the SB case). In the previous sections, we suggested that the low-frequency unsteadiness of TSBs is closely linked to the shear characteristics of the flow (see also Fig. 6). Specifically, we found that the streamwise components of the global, SPOD, and resolvent modes align with the position of maximum shear. This was demonstrated through the vorticity of each TSB flow, which appears to determine the position and size of the mode responsible for the low-frequency motion, i.e., the large coherent structure shown in Figs. 6, 10, and 12. Moreover, we indicated that the cutoff frequency of the observed low-frequency dynamics may be inversely proportional to the TSB size. A similar trend can be observed in the experimental work of Le Floc'h *et al.* [37], where the center of the low-frequency hump of the premultiplied PSD of the unsteady wall-pressure (close to max. APG) can be estimated at ∼3, 2, and 0.5 Hz for the small, medium, and large TSB flows, respectively [see Fig. 11(b)]. This observation implies that a meaningful scaling parameter should increase as the bubble size grows. Here, we consider the vorticity thickness of each numerical base flow

$$\delta_\omega(x) = \frac{\overline{U}_{\max}(x) - \overline{U}_{\min}(x)}{(\partial\overline{U}/\partial y)_{\max}}, \tag{9}$$

and depict it in Fig. 15(a) over the streamwise coordinate x. The scaling parameter is then chosen as the maximum value $\delta_{\omega,\max}$ for each flow configuration, resulting in a Strouhal number $\mathrm{St}_{\delta_\omega} = f\delta_{\omega,\max}/U_\infty$. Alternative scaling parameters, such as the displacement thickness δ^* and the momentum thickness Θ, were also considered. However, they did not yield a satisfactory collapse of the data.

To assess the proposed scaling, we compare the optimal gain of RA in the low-pass-filter representations $20\log(\sigma_1)$ across all cases (SB, MB, and LB) and $\beta^* = 0.25, 0.5, 1.0$, and 1.5 in Fig. 15(b). Note that only $\beta^* = 0.25$ is considered for the LB case (stable flow). We further subtract the maximum of each distribution, so that the -3dB line indicates the cutoff frequency of each curve. The cutoff frequencies of the gain distributions, which govern the low-frequency dynamics of the bubble, exhibit a reasonably consistent collapse across the spanwise wave number range $\beta^* = 0.25$–1.5 and all cases considered. This behavior is consistent with the broadband nature of low-frequency receptivity in TSBs, which is not associated with a sharply defined characteristic frequency. As such, alignment within a narrow frequency range is expected rather than an exact collapse onto a single frequency.

VII. CONCLUSIONS

In the present work, we extend the modal and nonmodal analysis of a PG-induced TSB [23] to a broader family of TSB flows characterized by varying separation extent—SB, MB, and LB. Our objective was to assess whether the low-frequency unsteadiness commonly observed in experimental flows featuring TSBs is governed by a common underlying mechanism across all investigated cases. To this end, we performed GLSA and RA on mean flows obtained from RANS simulations provided by Mohammed-Taifour *et al.* [38]. Significantly, the investigated small TSB flow does not exhibit mean flow separation, while the large TSB flow was found to be globally unstable in the asymptotic time limit. Nevertheless, experimental observations [37] on the same flow configuration reveal the persistence of broadband low-frequency unsteadiness even in the LB case.

The GLSA revealed strong similarities in mode structure, phase, and spectral characteristics across all cases within the spanwise wave number range of $\beta^* \sim 1$, even when the LB base flow was globally unstable. Notably, the dominant feature was a leading stationary mode, consistent with previous modal analyses of flows with separation bubbles [21,23,24,27,28]. RA, restricted to stable parameters, showed selective low-frequency receptivity for all considered cases, suggesting a common amplification mechanism within the family of TSB flows, regardless of separation extent ($L_b = 0$ m, SB) or stability characteristics ($\omega_i > 0$, LB). These findings support the hypothesis—proposed for subsonic TSBs in Ref. [23]—that low-frequency unsteadiness does not arise from self-sustained instability but from the forced response to a stationary, weakly damped eigenmode. In recent work, Sarras [36] further suggested that this mechanism may extend to marginally unstable flows, where the receptive mode remains close to criticality and thus retains amplifierlike characteristics. Here, we restrict ourselves to parameters for which the system is stable and demonstrate that the optimal response of RA aligns closely with the leading low-frequency SPOD mode based on TR-PIV measurements of the LB flow [37], with alignment values reaching up to 98%.

Given that similar stationary leading eigenmodes have been observed in several flows featuring separation bubbles, both in the subsonic [23,24,28] and supersonic [21,32,33] regimes, the proposed forced modal mechanism may extend to a broader class of separation bubble flows. While the emergence of a (weak) global instability in this study was found to be overshadowed by the forced dynamics of the flow, as suggested by Marquet *et al.* [28], it is conceivable that, under certain conditions, the stationary mode may rival or even dominate over the transient growth of disturbances. This may result in the formation of steady 3D structures, such as stall cells, as has been reported for the separated flow over airfoil wings in the laminar [27] and turbulent [34] regimes. Further work is required to investigate the link between the formation of steady or quasisteady stall cells and the low-frequency unsteadiness of TSBs. Here, we speculate that the global mode identified in the present work might be responsible for both phenomena.

The present results also have implications for future flow control strategies. Since we showed that the low-frequency unsteadiness of TSBs arises from a forced modal mechanism, detrimental effects related to this phenomenon may be mitigated by disrupting the forcing driving the phenomenon

(presumably related to nonlinear effects) or by modifying the base flow to weaken the amplification mechanism. Current work on the topic is ongoing [61].

ACKNOWLEDGMENT

This research was partially supported by the Deutscher Akademischer Austauschdienst (DAAD) - New Concepts for Sustainable, Green Aviation, Project No. 57705647.

DATA AVAILABILITY

The data that support the findings of this article are not publicly available because they are owned by a third party and the terms of use prevent public distribution. The data are available from the authors upon reasonable request.

APPENDIX A: VALIDATION OF EARSM BASE FLOW (MEDIUM BUBBLE)

In Sec. IV, we demonstrated that the modal and nonmodal analyses of the MB case, previously investigated by Cura *et al.* [23], can be reliably reproduced using the RANS mean flows from Mohammed-Taifour *et al.* [38]. However, minor discrepancies were observed, which are most likely attributed to the differences in the employed base flows, as these were not originally designed with the intention of direct comparability. In Fig. 16, we plot the streamwise component of the mean flows from the analysis conducted by Cura *et al.* [23] [Fig. 16(a)] and from the present work [Fig. 16(b)]. The mean flows are scaled using the bubble length L_b and the freestream velocity U_∞. The mean separation bubble is indicated by the $\overline{u} = 0$ contourline (white solid line), respectively. Clearly, the shear characteristics in the front part of the RANS TSB flow [Fig. 16(b)] differ quite a bit from the DNS [Fig. 16(a)], whereas the aft part of the bubble agrees well with the data of Coleman *et al.* [49]. However, as was previously stated, small changes in the position and size of the TSB seem to have a negligible effect on the modal and nonmodal characteristics of the flow (see also Figs. 3 and 4). For details on the agreement between the experimentally measured TSB flows and the numerically simulated RANS flows, see Mohammed-Taifour *et al.* [38]. The agreement between DNS data and experimental MB flow has been discussed in Le Floc'h *et al.* [37] and Cura *et al.* [23]. In Fig. 17, we compare the optimal response at low frequency St ≈ 0.01 for several spanwise wave numbers β. The streamwise and wall-normal component of the optimal response are shown in the

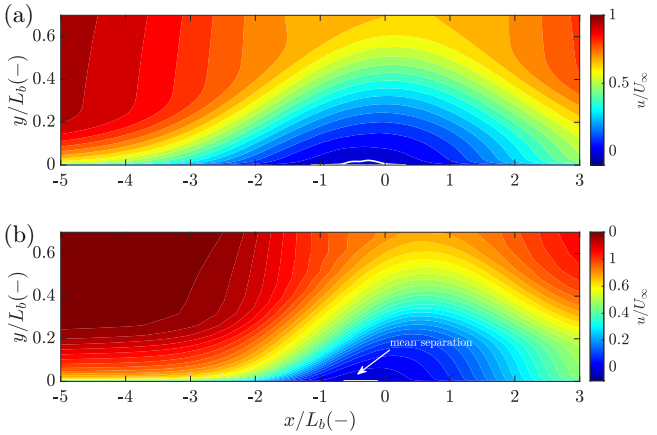


FIG. 16. Streamwise component of mean TSB flow from (a) DNS [49] and (b) RANS [38]. The flow is nondimensionalized using the length scale $l^* = L_b$ and the timescale $t^* = U_\infty/L_b$. The time-average location of the TSB is indicated by the $\overline{u} = 0$ contourline (white solid line).

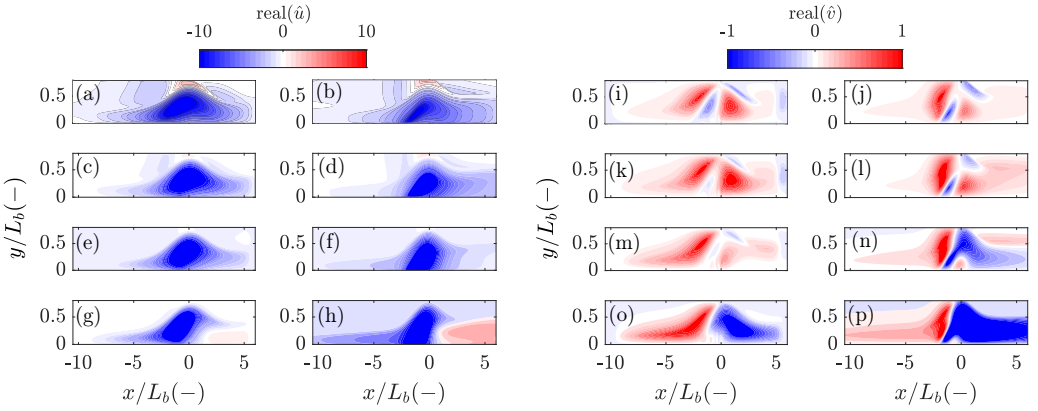


FIG. 17. Validation: Streamwise (left) and wall-normal (right) component of optimal response for different nondimensional spanwise wave numbers β. Results (a), (c), (e), (g) and (i), (k), (m), (o) previously presented in Ref. [23] and (b), (d), (f), (h) and (j), (l), (n), (p) from the current work are displayed. The spanwise wave number, from top to bottom, corresponds to $\beta = 0.5$, 1.5, 2.5, and 5. The Strouhal number is $\mathrm{St} = 0.01$.

left and right panels, respectively. Results obtained using the DNS base flow are shown in the first [Figs. 17(a), 17(c), 17(e), and 17(g)] and the third [Figs. 17(i), 17(k), 17(m), and 17(o)] columns, while those obtained based on RANS data are shown in the second [Figs. 17(b), 17(d), 17(f), and 17(h)] and last [Figs. 17(j), 17(l), 17(n), and 17(p)] columns, respectively.

APPENDIX B: LB BOUNDARY TREATMENT

In our previous work, satisfactory results were obtained using the available DNS domain, which had a wall-normal extent comparable to the small domain ($y_h = Y = 0.1\,\mathrm{m}$) used for the SB and MB cases in the present study (see also Fig. 16). However, when this small domain is applied to the LB case, the dominant shear regions are not fully contained within the computational domain, and confinement effects as well as mode distortion can be observed (not shown here). To address this, a larger wall-normal extent ($y_h = 0.15\,\mathrm{m}$) was used in the LB case, ensuring that the dominant flow structures are fully captured. Figure 18 demonstrates that this increased domain height has minimal influence on the growth rate of the leading GLSA modes over various spanwise wave numbers [Fig. 18(a)] and the spectral characteristics of the LNSE operator, represented by the eigenvalue spectrum at $\beta^* = 0.5$ [Fig. 18(b)].

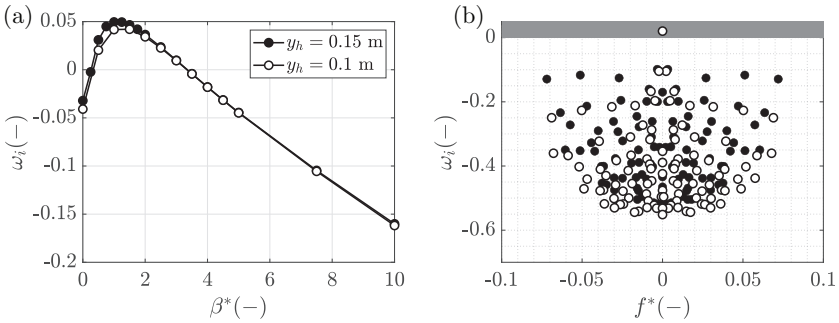


FIG. 18. (a) Growth rate of leading GLSA mode ω_i over spanwise wave number β^* and (b) eigenvalue spectrum for $\beta^* = 0.5$. Results using the tall domain $y_h = 0.15\,\mathrm{m}$ and the small domain $y_h = Y = 0.1\,\mathrm{m}$ are depicted. The unstable domain is indicated by the gray-shaded region.

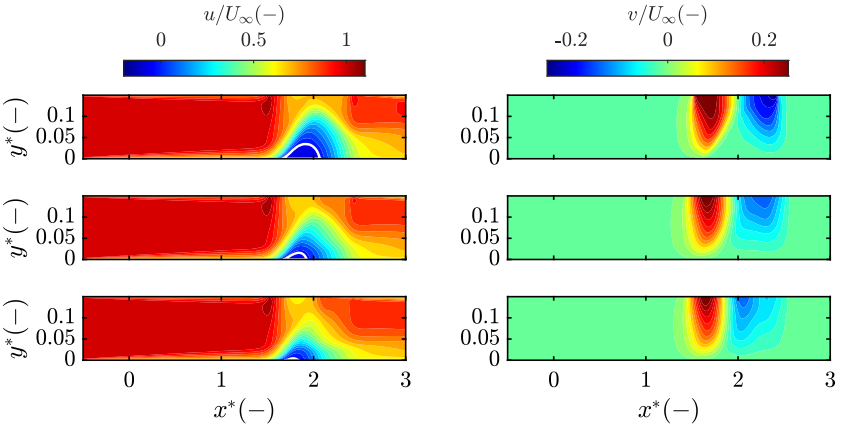


FIG. 19. Streamwise (left) and wall-normal (right) component of exemplary synthetic base flows for $\kappa = 0.9$ (top), $\kappa = 0.6$ (center), and $\kappa = 0.3$ (bottom).

APPENDIX C: SYNTHETIC BASE FLOWS

To assess the synthetic base flows used for the modal analysis in Sec. V B, representative flows are depicted in Fig. 19. The streamwise (left) and wall-normal (right) component are displayed for blending factors $\kappa = 0.9$ (top), $\kappa = 0.6$ (center), and $\kappa = 0.3$ (bottom). As can be seen, the linear combination of the MB case ($\kappa = 0$) and the LB case ($\kappa = 1$) following Eq. (5) produces smooth linear blends where the size of the TSB gradually increases (see the white contour line where $\overline{u} = 0$).

[1] M. Gaster, *The Structure and Behaviour of Laminar Separation Bubbles* (Her Majesty's Stationery Office, London, 1969).
[2] H. P. Horton, Laminar separation bubbles in two and three dimensional incompressible flow, Ph.D. thesis, Queen Mary University of London, 1968.
[3] M. Marquillie, and U. Ehrenstein, On the onset of nonlinear oscillations in a separating boundary-layer flow, J. Fluid Mech. **490**, 169 (2003).
[4] J. K. Eaton and J. P. Johnston, A review of research on subsonic turbulent flow reattachment, AIAA J. **19**, 1093 (1981).
[5] M. Kiya and K. Sasaki, Structure of a turbulent separation bubble, J. Fluid Mech. **137**, 83 (1983).
[6] J. M. Delery, Shock wave/turbulent boundary layer interaction and its control, Prog. Aerospace Sci. **22**, 209 (1985).
[7] Y. Na and P. Moin, Direct numerical simulation of a separated turbulent boundary layer, J. Fluid Mech. **374**, 379 (1998).
[8] D. G. Mabey, Analysis and correlation of data on pressure fluctuations in separated flow, J. Aircr. **9**, 642 (1972).
[9] A. Mohammed-Taifour and J. Weiss, Unsteadiness in a large turbulent separation bubble, J. Fluid Mech. **799**, 383 (2016).
[10] R. Richardson, Y. Zhang, L. N. Cattafesta, and W. Wu, Low frequency characteristics of a pressure-gradient induced turbulent separation bubble, in *AIAA SCITECH 2023 Forum* (2023), p. 0079.
[11] J. Weiss, B. Steinfurth, L. Chamard, A. Giani, and P. Combette, Spectral proper orthogonal decomposition of unsteady wall shear stress under a turbulent separation bubble, AIAA J. **60**, 2150 (2022).
[12] S. Wang and S. Ghaemi, Unsteady motions in the turbulent separation bubble of a two-dimensional wing, J. Fluid Mech. **948**, A3 (2022).

[13] D. S. Dolling, Fifty years of shock-wave/boundary-layer interaction research: What next? AIAA J. **39**, 1517 (2001).
[14] J.-P. Dussauge, P. Dupont, and J.-F. Debiève, Unsteadiness in shock wave boundary layer interactions with separation, Aerospace Sci. Technol. **10**, 85 (2006).
[15] N. T. Clemens and V. Narayanaswamy, Low-frequency unsteadiness of shock wave/turbulent boundary layer interactions, Annu. Rev. Fluid Mech. **46**, 469 (2014).
[16] D. V. Gaitonde, Progress in shock wave/boundary layer interactions, Prog. Aerospace Sci. **72**, 80 (2015).
[17] S. J. Beresh, N. T. Clemens, and D. S. Dolling, Relationship between upstream turbulent boundary-layer velocity fluctuations and separation shock unsteadiness, AIAA J. **40**, 2412 (2002).
[18] S. Piponniau, J.-P. Dussauge, J.-F. Debieve, and P. Dupont, A simple model for low-frequency unsteadiness in shock-induced separation, J. Fluid Mech. **629**, 87 (2009).
[19] S. Priebe, J. H. Tu, C. W. Rowley, and M. P. Martín, Low-frequency dynamics in a shock-induced separated flow, J. Fluid Mech. **807**, 441 (2016).
[20] W. Wu, C. Meneveau, and R. Mittal, Spatio-temporal dynamics of turbulent separation bubbles, J. Fluid Mech. **883**, A45 (2020).
[21] B. Bugeat, J.-Ch Robinet, J.-C. Chassaing, and P. Sagaut, Low-frequency resolvent analysis of the laminar oblique shock wave/boundary layer interaction, J. Fluid Mech. **942**, A43 (2022).
[22] J. Hao, On the low-frequency unsteadiness in shock wave–turbulent boundary layer interactions, J. Fluid Mech. **971**, A28 (2023).
[23] C. Cura, A. Hanifi, A. V. G. Cavalieri, and J. Weiss, On the low-frequency dynamics of turbulent separation bubbles, J. Fluid Mech. **991**, A11 (2024).
[24] V. Theofilis, S. Hein, and U. Dallmann, On the origins of unsteadiness and three-dimensionality in a laminar separation bubble, Philos. Trans. R. Soc. Lond. A **358**, 3229 (2000).
[25] D. Rodriguez and V. Theofilis, Structural changes of laminar separation bubbles induced by global linear instability, J. Fluid Mech. **655**, 280 (2010).
[26] D. Rodríguez, E. M. Gennaro, and M. P. Juniper, The two classes of primary modal instability in laminar separation bubbles, J. Fluid Mech. **734**, R4 (2013).
[27] D. Rodríguez and V. Theofilis, On the birth of stall cells on airfoils, Theor. Comput. Fluid Dyn. **25**, 105 (2011).
[28] O. Marquet, D. Sipp, J.-M. Chomaz, and L. Jacquin, Amplifier and resonator dynamics of a low-Reynolds-number recirculation bubble in a global framework, J. Fluid Mech. **605**, 429 (2008).
[29] F. Gallaire, M. Marquillie, and U. Ehrenstein, Three-dimensional transverse instabilities in detached boundary layers, J. Fluid Mech. **571**, 221 (2007).
[30] J.-C. Robinet, Bifurcations in shock-wave/laminar-boundary-layer interaction: Global instability approach, J. Fluid Mech. **579**, 85 (2007).
[31] E. Touber and N. D. Sandham, Large-eddy simulation of low-frequency unsteadiness in a turbulent shock-induced separation bubble, Theor. Comput. Fluid Dyn. **23**, 79 (2009).
[32] S. Pirozzoli, J. Larsson, J. W. Nichols, M. Bernardini, B. E. Morgan, and S. K. Lele, Analysis of unsteady effects in shock/boundary layer interactions, in *Proceedings of the Summer Program* (Center for Turbulence Research, 2010), pp. 153–164.
[33] J. W. Nichols, J. Larsson, M. Bernardini, and S. Pirozzoli, Stability and modal analysis of shock/boundary layer interactions, Theor. Comput. Fluid Dyn. **31**, 33 (2017).
[34] K. Sarras, C. Tayeh, V. Mons, and O. Marquet, Linear stability analysis of turbulent mean flows based on a data-consistent Reynolds-averaged Navier-Stokes model: Prediction of three-dimensional stall cells around an airfoil, J. Fluid Mech. **1001**, A41 (2024).
[35] K. J. Plotkin, Shock wave oscillation driven by turbulent boundary-layer fluctuations, AIAA J. **13**, 1036 (1975).
[36] K. Sarras, Global aerodynamic and aeroelastic instabilities of airfoils near stall, Ph.D. thesis, Institut Polytechnique de Paris, 2025.
[37] A. Le Floc'h, J. Weiss, A. Mohammed-Taifour, and L. Dufresne, Measurements of pressure and velocity fluctuations in a family of turbulent separation bubbles, J. Fluid Mech. **902**, A13 (2020).

[38] A. Mohammed-Taifour, J. Weiss, and L. Dufresne, Explicit algebraic Reynolds-stress modeling of pressure-induced separating flows in the presence of sidewalls, J. Fluids Eng. **143**, 101502 (2021).
[39] S. Wallin and A. V. Johansson, An explicit algebraic Reynolds stress model for incompressible and compressible turbulent flows, J. Fluid Mech. **403**, 89 (2000).
[40] F. R. Menter, Two-equation eddy-viscosity turbulence models for engineering applications, AIAA J. **32**, 1598 (1994).
[41] B. J. McKeon and A. S. Sharma, A critical-layer framework for turbulent pipe flow, J. Fluid Mech. **658**, 336 (2010).
[42] W. C. Reynolds and A. K. M. F. Hussain, The mechanics of an organized wave in turbulent shear flow. Part 3. Theoretical models and comparisons with experiments, J. Fluid Mech. **54**, 263 (1972).
[43] B. Pier, On the frequency selection of finite-amplitude vortex shedding in the cylinder wake, J. Fluid Mech. **458**, 407 (2002).
[44] D. Barkley, Linear analysis of the cylinder wake mean flow, Europhys. Lett. **75**, 750 (2006).
[45] O. T. Schmidt, A. Towne, T. Colonius, A. V. G. Cavalieri, P. Jordan, and G. A. Brès, Wavepackets and trapped acoustic modes in a turbulent jet: Coherent structure eduction and global stability, J. Fluid Mech. **825**, 1153 (2017).
[46] D. Edgington-Mitchell, T. Wang, P. Nogueira, O. Schmidt, V. Jaunet, D. Duke, P. Jordan, and A. Towne, Waves in screeching jets, J. Fluid Mech. **913**, A7 (2021).
[47] L. I. Abreu, A. Tanarro, A. V. G. Cavalieri, P. Schlatter, R. Vinuesa, A. Hanifi, and D. S. Henningson, Spanwise-coherent hydrodynamic waves around flat plates and airfoils, J. Fluid Mech. **927**, A1 (2021).
[48] D. C. P. Blanco, E. Martini, K. Sasaki, and A. V. G. Cavalieri, Improved convergence of the spectral proper orthogonal decomposition through time shifting, J. Fluid Mech. **950**, A9 (2022).
[49] G. N. Coleman, C. L. Rumsey, and P. R. Spalart, Numerical study of turbulent separation bubbles with varying pressure gradient and Reynolds number, J. Fluid Mech. **847**, 28 (2018).
[50] D. A. Hammond and L. G. Redekopp, Local and global instability properties of separation bubbles, Eur. J. Mech. B Fluids **17**, 145 (1998).
[51] U. Rist and U. Maucher, Investigations of time-growing instabilities in laminar separation bubbles, Eur. J. Mech. B Fluids **21**, 495 (2002).
[52] S. S. Diwan and O. N. Ramesh, On the origin of the inflectional instability of a laminar separation bubble, J. Fluid Mech. **629**, 263 (2009).
[53] F. C. Lajús Jr., A. Sinha, A. V. G. Cavalieri, C. J. Deschamps, and T. Colonius, Spatial stability analysis of subsonic corrugated jets, J. Fluid Mech. **876**, 766 (2019).
[54] Z. Yuan, E. Alva, T. B. de Araújo, A. V. G. Cavalieri, and A. Hanifi, A numerical investigation of airfoil tonal noise reduction by roughness elements, J. Fluid Mech. **1015**, A11 (2025).
[55] A. Mohammed-Taifour and J. Weiss, Periodic forcing of a large turbulent separation bubble, J. Fluid Mech. **915**, A24 (2021).
[56] L. Lesshafft, O. Semeraro, V. Jaunet, A. V. G. Cavalieri, and P. Jordan, Resolvent-based modeling of coherent wave packets in a turbulent jet, Phys. Rev. Fluids **4**, 063901 (2019).
[57] L. I. Abreu, A. V. G. Cavalieri, P. Schlatter, R. Vinuesa, and D. S. Henningson, Spectral proper orthogonal decomposition and resolvent analysis of near-wall coherent structures in turbulent pipe flows, J. Fluid Mech. **900**, A11 (2020).
[58] A. Towne, O. T. Schmidt, and T. Colonius, Spectral proper orthogonal decomposition and its relationship to dynamic mode decomposition and resolvent analysis, J. Fluid Mech. **847**, 821 (2018).
[59] O. T. Schmidt and T. Colonius, Guide to spectral proper orthogonal decomposition, AIAA J. **58**, 1023 (2020).
[60] P. J. Schmid, D. S. Henningson, and D. F. Jankowski, Stability and transition in shear flows, Appl. Mech. Rev. **55**, B57 (2002).
[61] L. Fuchs, J. G. R. von Saldern, B. Steinfurth, J. Weiss, and K. Oberleithner, Resolvent modeling and control of standing-wave low-frequency dynamics of a turbulent separation bubble, in *2nd European Fluid Dynamics Conference, Dublin* (2025).